THE JOURNAL OF NAVIGATION (2019), **72**, 207–228.
doi:10.1017/S0373463318000589

Vertical Obstacle Avoidance and Navigation of Autonomous Underwater Vehicles with H∞ Controller and the Artificial Potential Field Method

Shun-Min Wang, Ming-Chung Fang and Cheng-Neng Hwang

(*Department of Systems & Naval Mechatronic Engineering, National Cheng-Kung University, Tainan, 70101, Taiwan*)
(E-mail: smwang@mail.ncku.edu.tw)

An H∞ controller combined with an Artificial Potential Field Method (APFM) was applied to seabed navigation for Autonomous Underwater Vehicles (AUVs), aimed particularly at obstacle avoidance and bottom-following operations in the vertical plane. Depth control and altitude control prevented the AUV from colliding with the sea bottom or with obstacles and prevented the AUV from diving beyond its maximum depth limit when bottom following. Simulation and laboratory trials with various seabed contours indicated that with the H∞ controller, the AUV was able to safely reach appointed destinations without collisions. Tests also showed that the H∞ controller was robust and suppressed interference, hence ensuring the precision of its navigation control. The proposed H∞ controller combined with the APFM has thus been proved to be both feasible and effective.

KEYWORDS

1. Autonomous underwater vehicle. 2. Artificial potential field method. 3. Obstacle avoidance. 4. H∞ controller.

Submitted: 28 April 2017. Accepted: 8 July 2018. First published online: 20 August 2018.

1. INTRODUCTION. Autonomous Underwater Vehicles (AUVs) are being used more and more. A typical AUV mission is seabed mapping with a side-scan sonar. To ensure the quality of map data, the trajectory of the AUV must be a straight line throughout the operation. The AUV can only avoid colliding with obstacles by adjusting course in the vertical plane. Another typical AUV mission is to follow the seabed at a fixed altitude, taking pictures with an optical camera for biological or other scientific investigations; for such missions, the AUV must avoid collisions during seabed-following navigation.

When navigating the AUV within the vertical plane, the depth and altitude must be considered. For example, when navigating at a fixed depth, aside from maintaining the depth, the distance to the seabed must be considered to ensure the AUV does not scrape the seabed if the terrain drastically changes. If the AUV moves too far from the seabed, the accuracy of data may be compromised because the side-scan sonar may fail to receive

echoes from the seabed. When steering an AUV at a fixed altitude, the depth of the AUV must be noted, particularly in proximity to a marine trench, lest the AUV dive below its maximum operating depth; conversely, when the water depth approaches zero, the AUV runs the risk of surfacing, which would subject it not only to the impact of winds and waves, but also to the danger of collision with surface vessels or floating objects.

In terms of real-time path planning and anti-collision navigation, numerous methods and techniques have been developed for unmanned ground vehicles. One of the most commonly used is the Artificial Potential Field Method (APFM), proposed by Khatib (1986). APFM is a simple, fast, and efficient algorithm. It requires no global search path planning and can react instantly to obstacles (Khosla and Volpe, 1988). However, this method has flaws, including the local minimum problem that occurs when the vehicle runs into a trap situation such as a U-shaped obstacle (Koren and Borenstein, 1991), and the problem of close proximity of an obstacle to a goal, which can cause the vehicle to become stuck or unable to reach the goal (Rimon and Koditschek, 1992). Some solutions have been advanced for these problems, such as enhanced potential functions (Ge and Cui, 2000; 2002), and improved algorithms (Yin and Yin, 2008; Gao et al., 2013).

In recent years, techniques for unmanned ground vehicles have gradually spread to AUVs; some researchers have explored the applications of the APFM. For example, Ding et al. (2005) proposed a path planning algorithm based on a virtual potential field, which performed in both simulations and experiments. Gao et al. (2008) proposed a potential field method for an AUV navigation controller; Saravanakumar and Asokan (2013) proposed a multipoint potential field method to solve the problem of local minima in three-dimensional AUV path planning and Cheng et al. (2015) integrated artificial potential fields with velocity synthesis algorithms, producing a path planning algorithm that enables effective avoidance of dynamic obstacles and the influence of ocean currents.

Although much headway has been made for AUV obstacle avoidance, most studies have concentrated on horizontal controls, and literature on vertical navigation has been relatively scant. However, vertical navigation is in fact more crucial in practice. Regarding vertical navigation, Antonelli et al. (2001) used an AUV to conduct seabed surveys at a fixed depth; Kanakakis et al. (2004) built modules based on actual parameters of AUVs and sonars and conducted depth-control simulations pertaining to changes in seabed terrain; Hanumant (1995) used an underwater altimeter to conduct bottom-following missions and Creuze and Jouvencel (2002) used depth data for collision avoidance.

In any event, the most vital aspect pertaining to obstacle avoidance and bottom following is controller design, and numerous studies have addressed controllers and AUV control strategies. For example, Kaminer et al. (1991) applied H∞ synthesis theory to the design of an AUV controller, and then evaluated its performance in simulations. Logan (1994) made a comparison between a synthesised H∞/μ controller and a sliding mode controller by conducting simulations and analyses with a nonlinear model of an AUV. Feng and Allen (2002) combined a linear matrix inequality approach to H∞ control theory with mixed weighted sensitivity functions for the design of an AUV controller and tested that controller in simulations. Moreira and Soares (2008) proposed H_2 and H∞ AUV controller designs and compared their performance and robustness levels in the presence of waves with a nonlinear model. Petrich and Stilwell (2011) proposed an H∞ controller design that addressed the structured uncertainty of coupling items, and tested its robustness, resistance to interference and efficacy through simulations and field trials.

https://doi.org/10.1017/S0373463318000589 Published online by Cambridge University Press

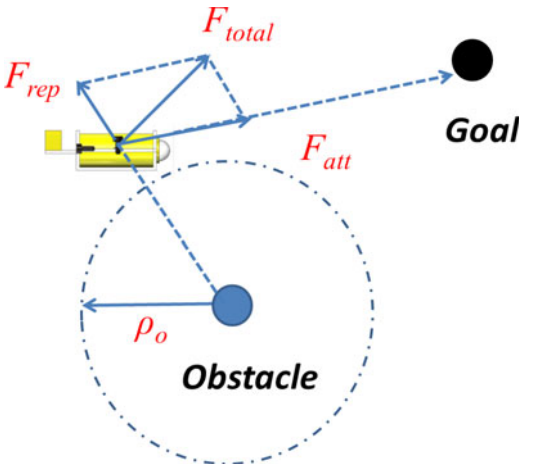

Figure 1. Artificial potential field.

This study has developed a robust AUV navigation controller. To ensure system stability and performance, H∞ control theory was adopted. APFM was incorporated for path planning, obstacle avoidance and accurate bottom following.

This article is organised as follows: Section 2 addresses the methodology, including the basic principles of APFM, algorithms for depth and altitude control and H∞ control theory; Section 3 addresses simulations and analyses; Section 4 addresses laboratory trials and Section 5 presents the conclusion.

2. METHODOLOGY.

2.1. *Basic principles of the artificial potential field method.* The APFM is a path planning algorithm introduced by Khatib (1986). With a simple numerical model suitable for real-time obstacle avoidance and navigation, the APFM has seen widespread use in unmanned ground vehicles. For AUV applications, a virtual potential field must be defined, in which the AUV, Goal, and Obstacle are treated as different points. The Goal has an attractive field, and the Obstacle has a repulsive field. As shown in Figure 1, the AUV moves towards the Goal under its attractive force, and away from the Obstacle under its repulsive force; thus, the AUV moves in the direction of the resultant (of the attractive and repulsive vectors).

Assuming the position of the AUV is $X_i = (x, y)$, the function for the Goal's attractive field can be defined as follows:

$$U_{att}(X_i) = \frac{1}{2}\alpha\rho^2(X_i, X_g) \tag{1}$$

The function for the Obstacle's repulsive field is as follows:

$$U_{rep}(X_i) = \begin{cases} \frac{1}{2}\beta\left(\frac{1}{\rho(X_i,X_o)} - \frac{1}{\rho_o}\right)^2 & \rho(X_i, X_o) \le \rho_0 \\ 0 & \rho(X_i, X_o) > \rho_0 \end{cases} \tag{2}$$

https://doi.org/10.1017/S0373463318000589 Published online by Cambridge University Press

where: α and β are the gain factors for the attractive force and repulsive force, respectively; X_i, X_g, and X_o are the spatial positions of the AUV, Goal and Obstacle, respectively; $\rho(X_i, X_g)$ and $\rho(X_i, X_o)$ are the spatial distances from the AUV to the Goal and Obstacle, respectively and ρ_o is the Obstacle's radius of influence on the AUV, which is not effective when the AUV is not within the repulsive field.

By calculating the negative gradient of the attractive and repulsive fields, the corresponding attractive function and repulsive function can be obtained as follows:

Attractive function:

$$F_{att}(X_i) = -\nabla U_{att}(X_i) = \alpha\rho(X_i, X_g) \tag{3}$$

Repulsive function:

$$\begin{aligned} F_{rep}(X_i) &= -\nabla U_{rep}(X_i) \\ &= \begin{cases} \beta\left(\frac{1}{\rho(X_i,X_o)} - \frac{1}{\rho_o}\right)\frac{1}{\rho^2(X_i,X_o)}, & \rho(X_i, X_o) \le \rho_0 \\ 0, & \rho(X_i, X_o) > \rho_0 \end{cases} \end{aligned} \tag{4}$$

Hence, the resultant force on the AUV is as follows:

$$F_{total}(X_i) = F_{att}(X_i) + F_{rep}(X_i) \tag{5}$$

The depth-control algorithm and altitude control algorithm for the AUV's obstacle avoidance and bottom-following operations are derived from these basic principles.

2.2. *Depth-control algorithm.* As per the APFM, the depth-control algorithm defines the attractive field as a depth function and the repulsive field as an altitude function, with a predetermined minimal safe altitude for obstacle avoidance. The AUV approximates a desired depth according to the resultant force of the attractive and repulsive forces, so as to prevent collisions with the seabed and obstacles. As shown in Figure 2, the virtual force only works along the z-axis. The desired depth defines an attractive field; the AUV is attracted to the desired depth; conversely, an obstacle has a repulsive field, whose repulsive force only works on the AUV when it comes into range; otherwise, the AUV will only be subjected to the attractive force. The depth-control function for the attractive potential field can be defined as (Gao et al., 2008):

$$U_{att}(z) = \begin{cases} k_{az}\,|z - z_d|\,, & |z - z_d| > l_z \\ \frac{k_{az}}{2l_z}\,(z - z_d)^2\,, & |z - z_d| \le l_z \end{cases} \tag{6}$$

where: z is the depth of the AUV; z_d is the desired depth; k_{az} is the gain value of the attractive force and l_z is the attraction switching condition such that, when the difference between z and z_d is larger than l_z, a linear function holds; otherwise, the standard quadratic function for the artificial potential field is used.

https://doi.org/10.1017/S0373463318000589 Published online by Cambridge University Press

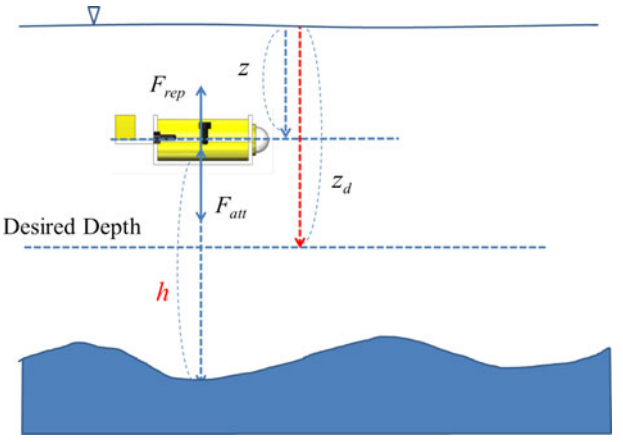

Figure 2. Depth control.

The attractive force is the negative gradient of the attractive potential field, and it can be defined as follows:

$$F_{att}(z) = -\nabla U_{att}(z) = \begin{cases} -k_{az}\ \mathrm{sgn}\,(z - z_d), & |z - z_d| > l_z \\ -\frac{k_{az}}{l_z}\,(z - z_d), & |z - z_d| \le l_z \end{cases} \tag{7}$$

When the AUV is close to the seabed, it is repelled by the repulsive field, defined as:

$$U_{rep}(h) = \begin{cases} \frac{1}{2}k_{rh}\left(\frac{1}{h} - \frac{1}{h_0}\right)^2, & 0 < h \le h_0 \\ 0, & h > h_0 \end{cases} \tag{8}$$

where: h is the altitude from the seabed to the AUV; k_{rh} is the gain value of the repulsive force and h_0 is the range of the repulsive field. When $h > h_0$, the AUV is out of range of the repulsive force.

The repulsive force is the negative gradient of the repulsive potential field; it can be defined as follows:

$$F_{rep}(h) = -\nabla U_{rep}(h) = \begin{cases} k_{rh}\left(\frac{1}{h} - \frac{1}{h_o}\right)\frac{1}{h^2}, & 0 < h \le h_0 \\ 0, & h > h_0 \end{cases} \tag{9}$$

Combining the attractive and repulsive forces yields the resultant force:

$$F_{total} = F_{att}(z) + F_{rep}(h) \tag{10}$$

The AUV controls its depth according to the resultant force, which can be defined as the following function:

$$z_{com} = k_z F_{total} \tag{11}$$

https://doi.org/10.1017/S0373463318000589 Published online by Cambridge University Press

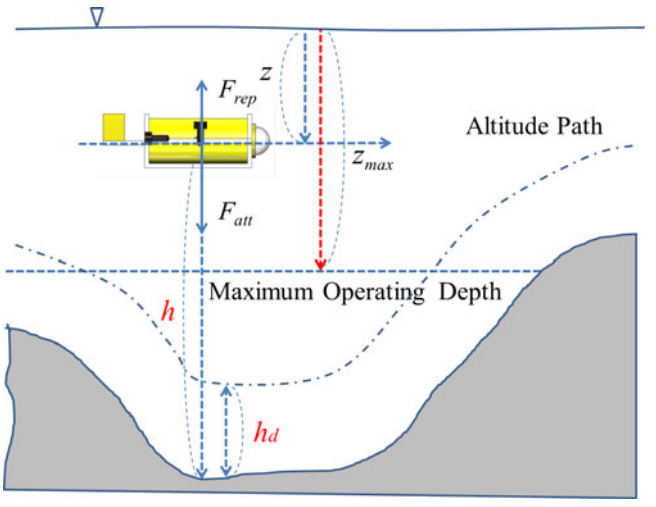

Figure 3. Altitude control.

where z_{com} is the depth-control command for the AUV, and k_z is the scale factor for the depth-control command.

2.3. *Altitude-control algorithm.* The altitude-control algorithm defines the attractive field as an altitude function, and the repulsive field a depth function, with a predetermined maximum operating depth for the AUV. The AUV maintains its altitude according to the resultant force it is subjected to, so that when the AUV conducts bottom following at a fixed altitude, it will not descend lower than a structurally safe depth.

As shown in Figure 3, h_d represents the desired altitude for the AUV bottom following. The AUV moves to h_d because h_d attracts the AUV. The maximum operating depth is defined as a repulsive field, which prevents the AUV from descending below its depth limit.

The altitude-control attractive function can be defined as (Gao et al., 2008):

$$U_{att}(h) = \begin{cases} k_{ah} \left| h - h_d \right|, & \left| h - h_d \right| > l_h \\ \frac{k_{ah}}{2l_h} (h - h_d)^2, & \left| h - h_d \right| \le l_h \end{cases} \tag{12}$$

where: h_d is the desired altitude; k_{ah} is the gain value of the attractive force, and l_h is the condition for the switching of the attractive function. When the difference between h and h_d is larger than l_h, the attractive function is linear; otherwise, it is a standard quadratic function for the artificial potential field.

The attractive force is the negative gradient of the attractive field, and it can be defined as follows:

$$\begin{aligned} F_{att}(h) &= -\nabla U_{att}(h) \\ &= \begin{cases} -k_{ah} \mathrm{sgn}\,(h - h_d), & \left| h - h_d \right| > l_h \\ -\frac{k_{ah}}{l_h} (h - h_d), & \left| h - h_d \right| \le l_h \end{cases} \end{aligned} \tag{13}$$

In light of the structural strength of the AUV, its maximum operating depth must be adopted as the repulsive field, to prevent the AUV from diving below its depth limit. The

https://doi.org/10.1017/S0373463318000589 Published online by Cambridge University Press

repulsive function can be defined as (Gao et al., 2008):

$$U_{rep}(z) = \begin{cases} \frac{k_{rz}}{2}\left(\frac{1}{z_{\max}-z} - \frac{1}{r_0}\right)^2, & 0 < z_{\max} - z \le r_o \\ 0, & z_{\max} - z > r_0 \end{cases} \tag{14}$$

where: z_{max} is the maximum operating depth; k_{rz} is the gain value of the repulsive force and r_0 is the radius of the repulsive field.

The repulsive force is defined as:

$$\begin{aligned} F_{rep}(z) &= -\nabla U_{rep}(z) \\ &= \begin{cases} -k_{rz}\left(\frac{1}{(z_{\max}-z)} - \frac{1}{r_0}\right)\frac{1}{(z_{\max}-z)^2}, & 0 < z_{\max} - z \le r_0 \\ 0, & z_{\max} - z > r_0 \end{cases} \end{aligned} \tag{15}$$

The resultant force on the AUV is shown as follows:

$$F_{total} = F_{att}(h) + F_{rep}(z) \tag{16}$$

As the AUV maintains its altitude according to the resultant force, the operation can be represented by a simple linear function as follows:

$$h_{com} = k_h F_{total} \tag{17}$$

where h_{com} is the altitude-control command for the AUV and k_h is the scale factor for the altitude-control command.

2.4. *H∞ control theory.* Obstacle avoidance and seabed following must be planned with the APFM and conducted with the H∞ controller, because the H∞ controller's robustness allows it to suppress external interference, maintain system stability and sustain precise control. The H∞ controller allows the minimal ∞ norm for the transfer function from the exogenous inputs and the controlled outputs and stabilises the entire closed-loop system. The ∞ norm can be defined as follows (Doyle et al., 1989):

$$\|G\|_\infty \equiv \sup_\omega \bar{\sigma}[G(j\omega)] \tag{18}$$

where: $G(s)$ is the transfer function of the system; *sup* is the least upper bound; and $\bar{\sigma}$ is the maximum singular value of $G(s)$, which is the least upper bound of the transfer function's maximum singular values for all frequencies.

The equations of state for this linear time-invariant system $G(s)$ are as follows:

$$\begin{aligned} \dot{X}(t) &= AX(t) + Bu(t) \\ y_S(t) &= CX(t) + Du(t) \end{aligned} \tag{19}$$

https://doi.org/10.1017/S0373463318000589 Published online by Cambridge University Press

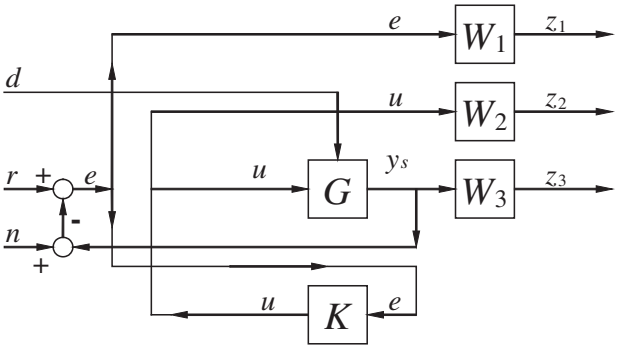

Figure 4. Augmented system.

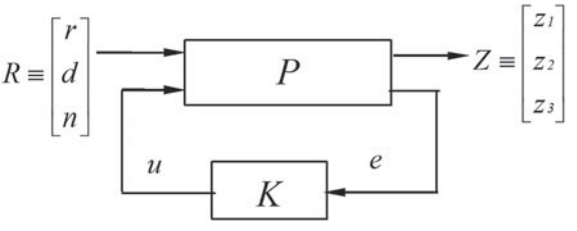

Figure 5. Standard control framework.

where: X is the system's state variables; u is the control input; y_s is the plant output; and A, B, C and D are constant matrices. Three weight functions are added to the system to form an augmented system $P(s)$ as shown in Figure 4, in which the three weight functions are defined as follows:

$$W_1 = \begin{bmatrix} A_{W1} & B_{W1} \\ C_{W1} & D_{W1} \end{bmatrix}, \quad W_2 = \begin{bmatrix} A_{W2} & B_{W2} \\ C_{W2} & D_{W2} \end{bmatrix}, \quad W_3 = \begin{bmatrix} A_{W3} & B_{W3} \\ C_{W3} & D_{W3} \end{bmatrix} \tag{20}$$

This augmented system can be expressed in a standard control framework, as shown in Figure 5, where the controlled output $Z(t)$ includes the tracking error $e(t)$, control input $u(t)$, and plant output $y_s(t)$; and the exogenous input $R(t)$ includes the reference signal $r(t)$, external interference $d(t)$ and sensor noise $n(t)$. The controlled output and exogenous input can be expressed as follows:

$$R(t) \equiv \begin{bmatrix} r(t) \\ d(t) \\ n(t) \end{bmatrix}, \quad z(t) \equiv \begin{bmatrix} z_1(t) \\ z_2(t) \\ z_3(t) \end{bmatrix} = \begin{bmatrix} W_1 e(t) \\ W_2 u(t) \\ W_3 y_S(t) \end{bmatrix} \tag{21}$$

https://doi.org/10.1017/S0373463318000589 Published online by Cambridge University Press

The augmented system can be expressed as a state matrix:

$$\begin{bmatrix} \dot{X} \\ \dot{X}_{W_1} \\ \dot{X}_{W_2} \\ \dot{X}_{W_3} \\ z_1 \\ z_2 \\ z_3 \\ e \end{bmatrix} = \begin{bmatrix} A & 0 & 0 & 0 & 0 & B \\ -B_{W_1} & A_{W_1} & 0 & 0 & B_{W_1} & -B_{W_1}D \\ 0 & 0 & A_{W_2} & 0 & 0 & B_{W_2} \\ B_{W_3}C & 0 & 0 & A_{W_3} & 0 & B_{W_3}D \\ -D_{W_1}C & C_{W_1} & 0 & 0 & D_{W_1} & -D_{W_1}D \\ 0 & 0 & C_{W_2} & 0 & 0 & D_{W_2} \\ D_{W_3}C & 0 & C_{W_3} & 0 & 0 & D_{W_3}D \\ -C & 0 & 0 & 0 & I & -D \end{bmatrix} \begin{bmatrix} X \\ X_{W_1} \\ X_{W_2} \\ X_{W_3} \\ R \\ u \end{bmatrix} \tag{22}$$

which can be simplified into the following:

$$\begin{bmatrix} \dot{X}(t) \\ Z(t) \\ e(t) \end{bmatrix} = \begin{bmatrix} A & B_1 & B_2 \\ C_1 & D_{11} & D_{12} \\ C_2 & D_{21} & D_{22} \end{bmatrix} \begin{bmatrix} X(t) \\ R(t) \\ u(t) \end{bmatrix} \tag{23}$$

where A, B_1, B_2, C_1, C_2, D_{11}, D_{12}, D_{21} and D_{22} are all constant matrices.

It can then be reformed as follows:

$$\begin{bmatrix} z_1 \\ z_2 \\ z_3 \\ \cdots \\ e \end{bmatrix} = \left[\begin{array}{cccc} W_1 & -W_1G & -W_1 & -W_1G \\ 0 & 0 & 0 & W_2 \\ 0 & W_3G & 0 & W_3G \\ \cdots & \cdots & \cdots & \cdots \\ I & -G & -I & -G \end{array}\right] \begin{bmatrix} r \\ d \\ n \\ \cdots \\ u \end{bmatrix} \tag{24}$$

or simplified to:

$$\begin{bmatrix} Z(s) \\ \cdots \\ e(s) \end{bmatrix} = \left[\begin{array}{c|c} P_{11}(s) & P_{12}(s) \\ \hline P_{21}(s) & P_{22}(s) \end{array}\right] \begin{bmatrix} R(s) \\ \cdots \\ u(s) \end{bmatrix} \tag{25}$$

As the transfer function $u(s) = K(s) \cdot e(s)$, this gives the following relations:

$$Z(s) = P_{11}(s) \cdot R(s) + P_{12}(s) \cdot K(s) \cdot e(s) \tag{26}$$

$$e(s) = P_{21}(s) \cdot R(s) + P_{22}(s) \cdot K(s) \cdot e(s) \tag{27}$$

$$\Rightarrow e(s) = (I - P_{22}(s) \cdot K(s))^{-1} P_{21}(s) \cdot R(s) \tag{28}$$

Substituting Equation (28) into Equation (26) yields:

$$Z = [P_{11} + P_{12} \cdot K (I - P_{22} \cdot K)^{-1} P_{21}] \cdot R \tag{29}$$

The linear fraction transformation $F_1(P, K)$ of the transfer function from $R(s)$ to $Z(s)$ can be expressed as follows:

$$F_l(P, K) = P_{11} + P_{12}K [I - P_{22}K]^{-1} P_{21} \tag{30}$$

The H∞ controller allows the minimal H∞ norm for the transfer function $F_l(P, K)$ from the exogenous inputs and the controlled outputs; it stabilises the entire closed-loop system.

https://doi.org/10.1017/S0373463318000589 Published online by Cambridge University Press

Therefore, for the H∞ norm for the transfer function $F_l(P,K)$, a value smaller than γ should be defined as follows:

$$\|F_l(P,K)\|_\infty = \sup_{\omega(t)} \frac{\|Z\|_2}{\|R\|_2} < \gamma \tag{31}$$

Usually γ is a value smaller than one and bears the physical meaning that the energy ($\|R\|_2$) of the exogenous input is transformed by the controller, and the energy ($\|Z\|_2$) of the system output is γ times lower than the input energy $\|R\|_2$.

Hwang (1993; 2002) proposed a polynomial approach to the H∞ control problem. It is relatively simple and convenient in calculation, because it only requires the positive definite solutions of two Riccati equations. The system's equations of state are as follows:

$$\begin{aligned} \dot{X}(t) &= AX(t) + B_1 w(t) + B_2 u(t) \\ Z(t) &= C_1 X(t) + D_{12} u(t) \\ e(t) &= C_2 X(t) + D_{21} w(t) \end{aligned} \tag{32}$$

Polynomial approaches must meet the following conditions:

(i) (A, B_1) must be stabilisable, and (C_1, A) must be detectable;
(ii) (A, B_2) must be stabilisable, and (C_2, A) must be detectable;
(iii) $D_{12}^T D_{12} = I$, and $D_{21} D_{21}^T = I$.

To obtain the solution for the H∞ controller, the gain for state feedback control K_c and the observer gain K_f must be acquired first (Doyle et al., 1989; Hwang, 1993):

$$K_c = -\left(B_2^T k_\infty X + D_{12}^T C_1\right) \tag{33}$$

$$K_f = -\left(I - h_\infty k_\infty\right)^{-1} \left(h_\infty C_2^T + B_1 D_{21}^T\right) \tag{34}$$

where k_∞ and h_∞ are the positive definite solutions for the following Riccati equations, respectively:

$$\begin{aligned} &\left(A - B_2 D_{12}^T C_1\right)^T k_\infty + k_\infty \left(A - B_2 D_{12}^T C_1\right) + k_\infty \left(B_1 B_1^T - B_2 B_2^T\right) k_\infty \\ &\quad + C_1^T \left(I - D_{12} D_{12}^T\right) \left(I - D_{12} D_{12}^T\right) C_1 = 0 \end{aligned} \tag{35}$$

$$A_t h_\infty + h_\infty A_t^T + h_\infty \left(C_1^T C_1 - C_2^T C_2\right) h_\infty + B_{1t} B_{1t}^T = 0 \tag{36}$$

and:

$$A_t = A - B_1 D_{21}^T C_2, \quad B_{1t} = B_1 \left(I - D_{21}^T D_{21}\right) \tag{37}$$

Then, the optimal H∞ control is as follows:

$$K(s) = \left[\begin{array}{c|c} A + B_1 B_1^T k_\infty + B_2 K_c + K_f C_2 & -K_f \\ \hline K_c & 0 \end{array}\right] \tag{38}$$

For a standard feedback control system whose plant is $G(s)$ and whose controller is $K(s)$, the sufficient condition for its stability is as follows:

$$\|KG\|_\infty < 1 \tag{39}$$

The stability and performance of the closed-loop system can be defined by the sensitivity function $S = 1/(I + GK)$, power transfer function $P = K/(I + GK)$, and complementary

https://doi.org/10.1017/S0373463318000589 Published online by Cambridge University Press

Table 1. Specifications of the AUV.

$m = 60\,\text{kg}$	$W = 588{\cdot}6\,\text{N}$	$B = 588{\cdot}6\,\text{N}$
$I_x = 1{\cdot}089\,\text{kg-m}^2$	$Iy = 2{\cdot}109\,\text{kg-m2}$	$I_z = 2{\cdot}109\,\text{kg-m2}$
$I_{xz} = 0\,\text{kg-m2}$	$I_{xy} = 0\,\text{kg-m2}$	$I_{yz} = 0\,\text{kg-m2}$
$x_G = 0\,\text{m}$	$y_G = 0\,\text{m}$	$z_G = 0\,\text{m}$
$x_B = 0\,\text{m}$	$y_B = 0\,\text{m}$	$z_B = -0{\cdot}05\,\text{m}$

Table 2. Added Mass and Fluid Damping Coefficients.

Added Mass		Damping			
$X_{\dot{u}}$	$-72{\cdot}66$	X_u	$-59{\cdot}74$	$X_{u\|u\|}$	-80
$Y_{\dot{v}}$	$-53{\cdot}31$	Y_v	$-115{\cdot}5$	$Y_{v\|v\|}$	$-1{\cdot}099$
$Z_{\dot{w}}$	$-44{\cdot}63$	Z_w	$-100{\cdot}8$	$Z_{w\|w\|}$	$-154{\cdot}3$
$K_{\dot{p}}$	$-5{\cdot}232$	K_p	$-2{\cdot}115$	$K_{p\|p\|}$	$-2{\cdot}316$
$M_{\dot{q}}$	$-9{\cdot}111$	M_q	$-1{\cdot}301$	$M_{q\|q\|}$	$-14{\cdot}19$
$N_{\dot{r}}$	$-9{\cdot}255$	N_r	$-1{\cdot}778$	$N_{r\|r\|}$	$-14{\cdot}05$

sensitivity function $T = GK/(I + GK)$. Therefore, suitably designed weight functions that allow favourable singular values for sensitivity, complementary sensitivity and power transfer must be introduced to attain the required system performance, favourable robustness, tracking ability and noise elimination capacity. To this end, the following conditions must be satisfied:

$$\begin{aligned} \|SW_1\|_\infty &\le 1 \\ \|PW_2\|_\infty &\le 1 \\ \|TW_3\|_\infty &\le 1 \end{aligned} \tag{40}$$

3. SIMULATION ANALYSIS.

3.1. *AUV Motion in the vertical plane.* This study of AUV motion concentrates on the control for vertical movements and only the equations of the heave must be addressed (Fang et al., 2006; 2007).

$$\begin{aligned} &(m - Z_{\dot{w}})\dot{w} + my_G\dot{p} - mx_G\dot{q} \\ &\quad = mz_G(p^2 + q^2) - mr(x_Gp + y_Gq) + q(m - X_{\dot{u}})u - p(m - Y_{\dot{v}})v \\ &\qquad + (Z_w + Z_{w|w|}\,|w|)w + (W - B)\cos\theta\cos\phi + F_z \end{aligned} \tag{41}$$

where: the inertia and added mass term is $(m - Z_{\dot{w}})\dot{w} + my_G\dot{p} - mx_G\dot{q}$; the centripetal force term is $mz_G(p^2 + q^2) - mr(x_Gp + y_Gq)$; the Coriolis force term is $q(m - X_{\dot{u}})u - p(m - Y_{\dot{v}})v$; the damping force term is $(Z_w + Z_{w|w|}\,|w|)w$; the restoring force term is $(W - B)\cos\theta\cos\phi$ and the external force term is F_z.

A self-developed AUV has been designed and built at the Cheng Kung University, which is $1{\cdot}1 \times 0{\cdot}385 \times 0{\cdot}35\,\text{m}$ in size. The specifications of the AUV are listed in Table 1, and the hydrodynamic coefficients for added mass and damping measured through the Planar Motion Mechanism (PMM) are as listed in Table 2 (Fang et al., 2015).

In Tables 1 and 2, m is the mass; W is the weight; B is the buoyancy; I_x, I_y, I_z, I_{xy} and I_{yz} are the inertia moments; $\dot{u}$, $\dot{v}$, $\dot{w}$, $\dot{p}$, $\dot{q}$ and $\dot{r}$ are the linear accelerations and

https://doi.org/10.1017/S0373463318000589 Published online by Cambridge University Press

angular accelerations along the three axes of the body coordinate system; $X_{\dot{u}}$, $Y_{\dot{v}}$, $Z_{\dot{w}}$, $K_{\dot{p}}$, $M_{\dot{q}}$ and $N_{\dot{r}}$ are the hydrodynamic coefficients of added mass; X_u, Y_v, Z_w, K_p, M_q and N_r are the linear damping coefficients; $X_{u|u|}$, $Y_{v|v|}$, $Z_{w|w|}$, $K_{p|p|}$, $M_{q|q|}$ and $N_{r|r|}$ are the quadratic damping coefficients and F_x, F_z and M_z are the horizontal axial thrust, vertical axial thrust, and horizontal turning moment, respectively. The centre of gravity is (x_G, y_G, z_G) and the centre of buoyancy is (x_B, y_B, z_B).

3.2. *Design of the H∞ controller.* By substituting the specifications and coefficients of the AUV in Tables 1 and 2 into the aforementioned dynamic equation, it can be simplified into the following matrices:

$$\begin{bmatrix} \dot{w} \\ \dot{z} \end{bmatrix} = \begin{bmatrix} -0.96 - 1.47\,|w| & 0 \\ 1 & 0 \end{bmatrix} \begin{bmatrix} w \\ z \end{bmatrix} + \begin{bmatrix} 0.0095 \\ 0 \end{bmatrix} F_z$$
$$y_d = \begin{bmatrix} 0 & 1 \end{bmatrix} \begin{bmatrix} w \\ z \end{bmatrix} \tag{42}$$

where the state variables are w and z, which are the rate of diving and depth of the AUV, respectively; F_z is the control input and y_d is the measurement output.

We set the weight functions W_1, W_2 and W_3 as:

$$W_1 = \frac{10}{100s + 1}, \quad W_2 = \frac{1}{1000}, \quad W_3 = \frac{s + 550}{300s + 800} \tag{43}$$

The original system is augmented with those weight functions; the gain for state feedback control K_{cl} and the observer gain K_{fl} can be obtained from the MATLAB simulation as follows:

When $\gamma = 0.9758$,

$$K_{c1} = \begin{bmatrix} 2233 & -981 & -2652 & -476 \end{bmatrix}$$
$$K_{f1} = \begin{bmatrix} -0.4384 & 0 & 0.0351 & 0.0132 \end{bmatrix}^T$$

the robust controller is:

$$K(S) = \begin{bmatrix} ak & bk \\ ck & dk \end{bmatrix} \tag{44}$$

where:

$$ak = \begin{bmatrix} -0.01 & 0 & 0 & 0 \\ 9.298 & -5.045 & -11.043 & -1.983 \\ 0 & 1 & -0.08 & 0.211 \\ 0 & 0 & 0.97 & -2.587 \end{bmatrix}, \quad bk = \begin{bmatrix} 0.4384 \\ 0 \\ -0.0351 \\ -0.0132 \end{bmatrix}$$
$$ck = \begin{bmatrix} 2233 & -981 & -2652 & -476 \end{bmatrix}, \quad dk = [0]$$

Then, the transfer function for the robust controller $K(s)$ can be expressed as:

$$K(s) = \frac{1078\,s^3 + 3912\,s^2 + 2766\,s + 4.031}{s^4 + 7.722\,s^3 + 24.58\,s^2 + 30.75\,s + 0.3051}$$
$$= \frac{1078.16(s + 2.667)(s + 0.96)(s + 0.00146)}{(s + 2.885)(s + 0.01)(s^2 + 4.827s + 10.58)}$$

https://doi.org/10.1017/S0373463318000589 Published online by Cambridge University Press

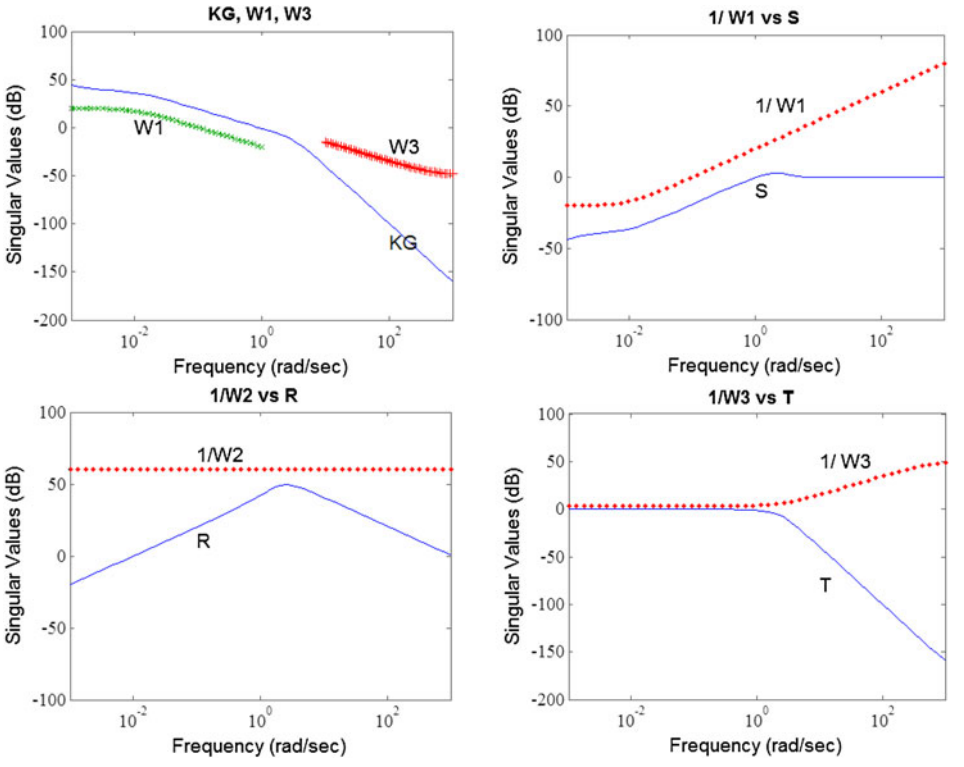

Figure 6. Results of frequency-domain response simulations for the H∞ controller.

3.3. *Frequency-domain response simulation.* The depth-control frequency-domain response simulation of the H∞ controller yielded the relationship between weight and singular values of system sensitivity shown in Figure 6. The open-loop system KG satisfies the restrictions of W_1 at low frequencies and the restrictions of W_3 at high frequencies. After W_1 had been determined, the singular values of its sensitivity function were under the reciprocal of W_1 (i.e. W_1^{-1}), satisfying the requirements for bottom following. When W_2 was set to be constant and the capacity of the thrusters was restricted, the curve of the singular values showed that the singular values of power transfer function R were under the reciprocal of W_2 (i.e. W_2^{-1}), satisfying the requirements. The power function R was able to prevent system saturation. After W_3 had been determined, the singular values of the complementary sensitivity function were all under the reciprocal of W_3 (i.e. W_3^{-1}), meaning the system resisted noise. Because the noise received by the sensor mostly originated from high-frequency signals, such as electromagnetic interference phenomena and the AUV's vibrations, the complementary sensitivity function T must generate low values at high frequencies to counteract noise.

3.4. *Noise interference simulation.* In a noise interference simulation, the performance of an H∞ controller and a Proportional Integral Derivative (PID) controller were compared; both were based on the system dynamics of the AUV and underwent adequate parameter adjustments. Figures 7(a), 7(c) and 7(e) show the contrast after adding an external interference signal *2sin(t)*; the H∞ controller was robust and was only

https://doi.org/10.1017/S0373463318000589 Published online by Cambridge University Press

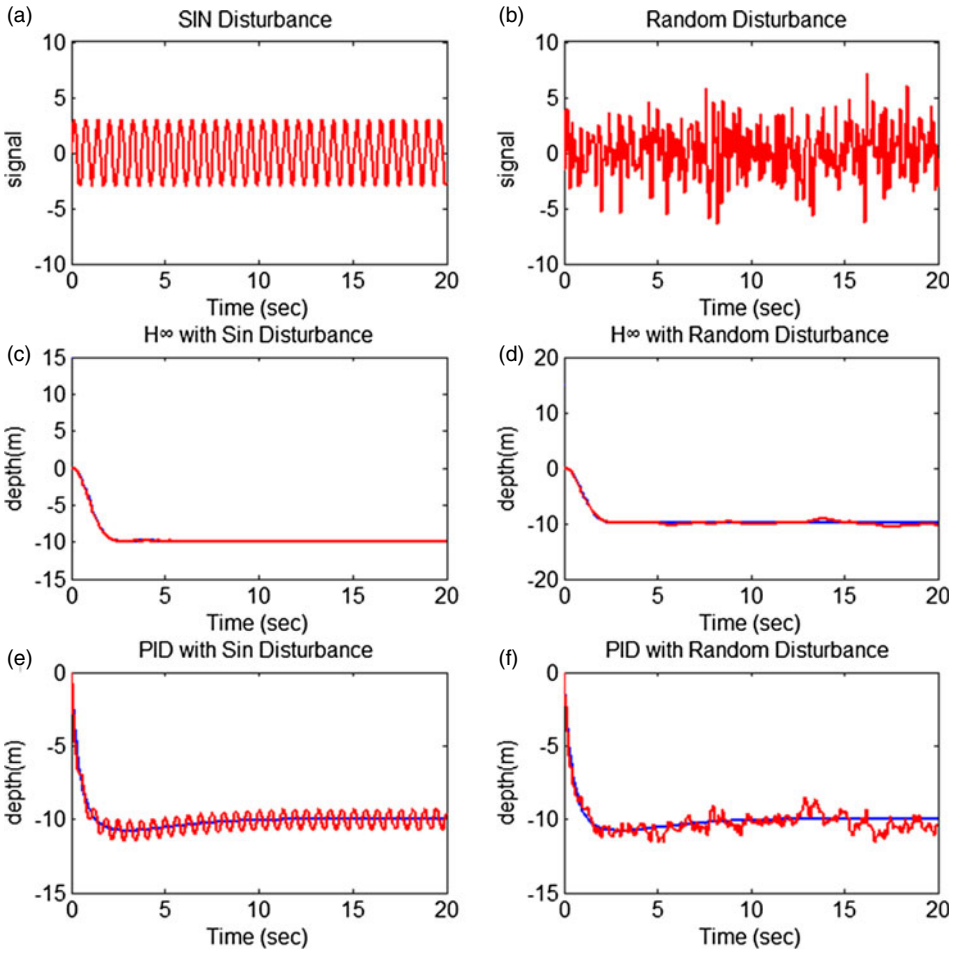

Figure 7. Comparison of the H∞ controller and PID controller under external interference.

slightly influenced by the interference, unlike the PID controller, which jittered noticeably. Figures 7(b), 7(d) and 7(f) show the addition of random interference, which also corroborated the robustness of the H∞ controller.

3.5. *Control simulation.* Owing to the varying contours of the seabed, the H∞ controller must issue different depth or altitude control commands for the AUV to conduct precision tracking. Simulations tested the depth control and altitude control algorithms:

3.5.1. *Depth control simulations.*

3.5.1.1. *Case 1: Obstacle avoidance at −5 m depth.* In this simulation, the AUV negotiated the varying contours of a seabed; conditions were as follows: AUV speed = 0·5 m/sec; k_{az} (gain value of the attractive force) = 0·5; l_z (condition for the switching of attractive function) = 2 m; k_{rh} (gain value of the repulsive force) = 0·8; h_0 (range of the repulsive field) = 5 m; and z_d (desired depth) = −5 m. In Figure 8, the black dashed line represents the seabed profile, the red solid line the AUV depth trajectory, and the blue dotted line the AUV altitude. Judging from the AUV depth trajectory (red line), initially,

https://doi.org/10.1017/S0373463318000589 Published online by Cambridge University Press

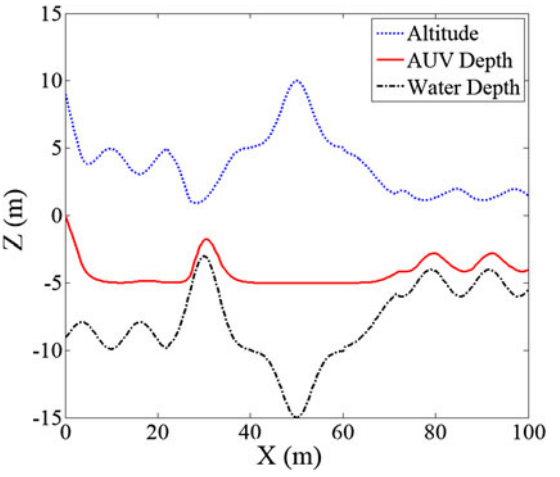

Figure 8. Obstacle avoidance simulation at −5 m depth.

the AUV was subjected to a constant attractive force and dived at a steady speed, until the difference between the AUV depth and the decided depth is not larger than 2 m, the attractive force acted by the standard quadratic function of the artificial potential field. At that moment, because the sea bottom was some distance away, the influence of the repulsive force was negligible and the AUV cruised at a fixed depth, until the rise of the seabed (x = 20∼30) caused an escalation in repulsive force, which in turn compelled the AUV to change its course and ascend, until it passed the obstacle and returned to the original desired depth.

3.5.1.2. *Case 2: Obstacle avoidance at −7 m depth.* In this simulation, the conditions were the same as those of Case 1, except that the desired depth was −7 m. Figure 9 presents the results. The AUV depth trajectory (red line) initially dived but reached the repulsive field before reaching the desired depth; as the AUV approached the bottom, the repulsive force surpassed the attractive force, and the resultant force compelled the AUV to adjust its depth; thus, it cruised above the seabed instead of crashing into it. Later, midway through the operation, the terrain became a downward slope, which increased the depth of the sea bottom and decreased the repulsive force; the attractive force again brought the AUV downward to the desired depth. When the terrain rose again, the escalating repulsive force compelled the AUV to climb up quickly to prevent collision, until it reached a shallow shelf, where it cruised at a fixed depth and accomplished the obstacle avoidance mission. The simulation results clearly indicate that the proposed APFM was able to maintain effective depth control and was able to keep the AUV above the bottom in shallow water, so as to prevent collision with the seabed. Additionally, it was able to quickly bring the AUV over a suddenly rising precipice. As for the problem of local minima, although the AUV was not able to reach any specified depth that was too close to the bottom, this apparent drawback is actually a feature because it serves as a safety measure that prevents the AUV from hitting the seabed.

3.5.2. *Altitude control simulations.*

3.5.2.1. *Case 1: Altitude control simulation at −15 m maximum operating depth.* The conditions for this altitude control simulation were set as follows: AUV speed = 0·5 m/sec;

https://doi.org/10.1017/S0373463318000589 Published online by Cambridge University Press

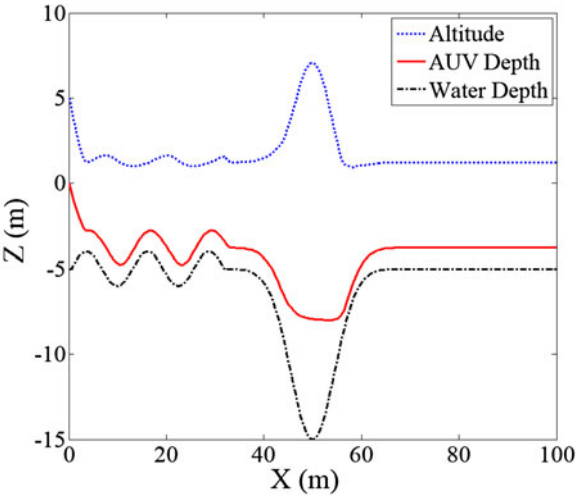

Figure 9. Obstacle avoidance simulation at −7 m depth.

h_d (desired altitude) = 2 m; k_{ah} (gain value of the attractive force) = 0·5; l_h (condition for the switching of attractive function) = 2 m; k_{rz} (gain value of the repulsive force)= 0·5; r_0 (range of the repulsive field) = 5 m and z_{max} (maximum operating depth) = −15 m. The simulation results are shown in Figure 10; initially, the AUV was only subjected to an attractive force and dived toward the desired altitude. When it reached the desired altitude, several metres remained between the desired altitude and maximum operational depth, thus the AUV was still outside of the range of the repulsive force; the attractive force was the only component of the resultant force on the AUV. From the course of the blue dotted line, which represents the cruising altitude of the AUV, it can be determined that the AUV cruised at a fixed altitude past the contours of the seabed; and according to the red solid line (depth of the AUV), the trajectory of the AUV also appeared to match perfectly with the profile of the seabed, indicating that the AUV was able to accomplish the bottom-following operation.

3.5.2.2. *Case 2: Altitude control simulation at −10 m maximum operating depth.*. The conditions for Case 2 were the same as those of Case 1, except that the maximum operating depth z_{max} = −10 m. As shown in Figure 11, when the AUV reached the middle section where the water was deeper than 10 m, the limit for the maximum operating depth exerted an increased repulsive force on the AUV, and the altered resultant force compelled the AUV to stop descending. According to the red line (depth trajectory), the AUV never dived beyond 10 m underwater, proving that the controller successfully prevented the AUV from exceeding the maximum operating depth.

4. LABORATORY TRIALS.

4.1. *Self-Developed AUV.* The self-developed AUV contained a power system and a control system in its waterproof hull. This consisted of four thrusters: two for surging and yawing, and the other two for heaving and rolling. It was equipped with a Doppler Velocity Log (DVL) to measure its speed, an inertial measurement unit for its attitude angles, a pressure gauge to measure its underwater depth and an underwater altimeter to measure its

https://doi.org/10.1017/S0373463318000589 Published online by Cambridge University Press

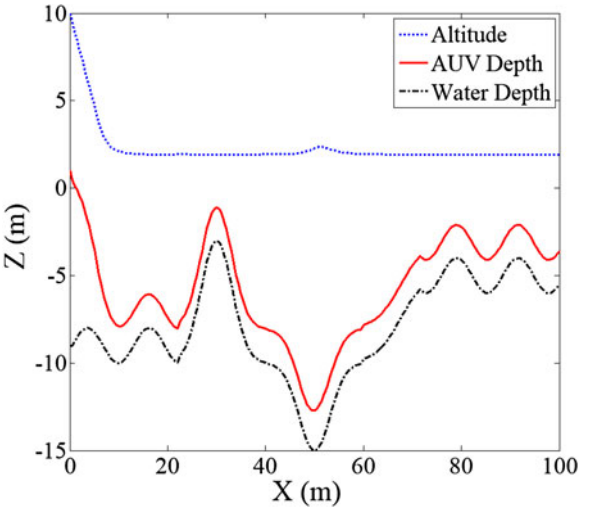

Figure 10. Bottom-following simulation at −15 m maximum operating depth.

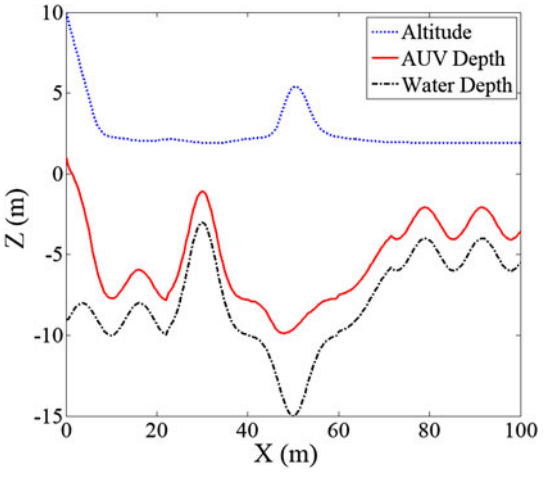

Figure 11. Bottom-following simulation at −10 m maximum operating depth.

distance to the seabed or an obstacle. The AUV carried three altimeters for the seabed and obstacles; they were installed parallel, perpendicular, and at 45° to the hull (Figure 12), for measuring the distance to any obstacle ahead (LF), to the sea bottom directly below (LH), and to the sea bottom at 45° ahead (LS), respectively.

The AUV used a CompactRIO (National Instruments) real-time controller as its primary hardware controller. The CompactRIO had Field Programmable Gate Array (FPGA) chips as processors; it was capable of parallel operations and was highly compatible with all types of sensors. The integrated LabVIEW graphical development platform enabled highly efficient customisation that allowed rapid deployment of the system. The trials were carried

https://doi.org/10.1017/S0373463318000589 Published online by Cambridge University Press

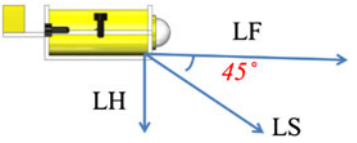

Figure 12. Orientations of the on board underwater altimeters.

Figure 13. Towing tank and underwater obstacle.

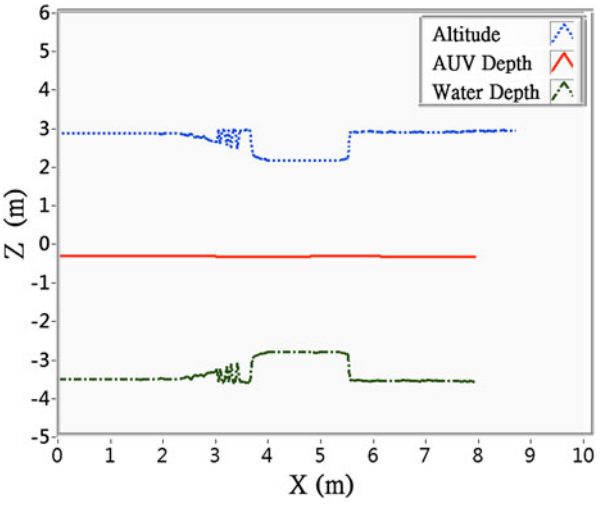

Figure 14. Bathymetric measurement results of the surface-cruising AUV.

out in the towing tank of the Department of Systems and Naval Mechatronic Engineering, National Cheng Kung University. The tank measured 165 × 8 × 4 m; a long desk was placed at the bottom as an obstacle (Figure 13). The desk measured 1·7 × 0·5 × 0·75 m.

4.2. *Bathymetric measurement.* For the measurement of water depth trial, the on board pressure gauge and underwater altimeter measured the depth and altitude, from which the water depth was calculated. From the DVL, the speed of the AUV was determined to be approximately 0·2 m/sec. The measured results are shown in Figure 14, with the blue dotted line representing the measured AUV altitude, the red solid line representing the AUV

https://doi.org/10.1017/S0373463318000589 Published online by Cambridge University Press

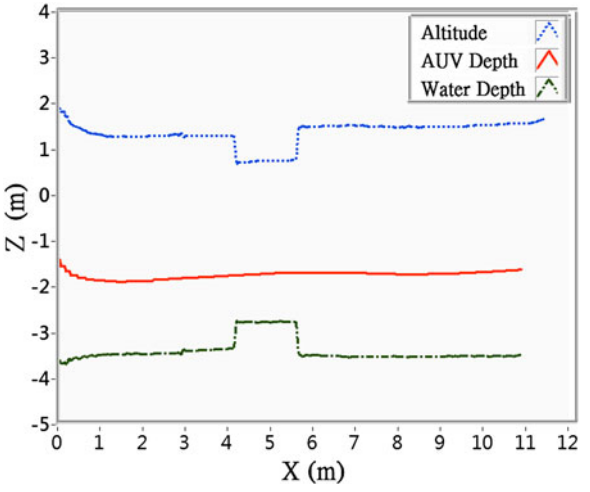

Figure 15. Depth control trial at desired depth of −1·7 m, without obstacle avoidance settings.

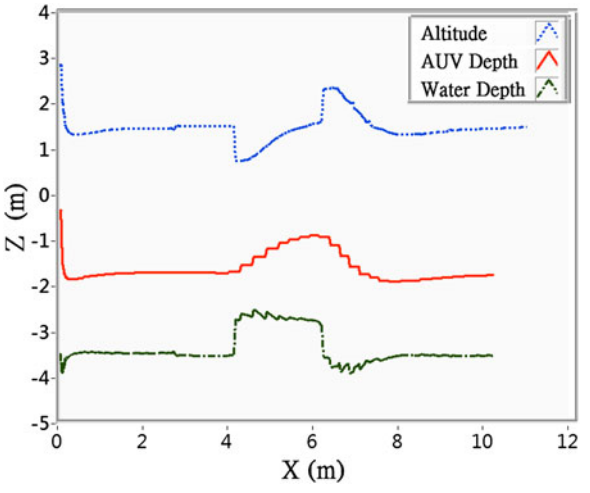

Figure 16. Depth control trial at desired depth of −1·7 m, with obstacle avoidance settings.

depth, and the black dashed line representing the measured water depth. The height of the underwater obstacle was calculated from this data.

4.3. *Depth control trial.* For comparison, a depth-control trial was conducted both with and without obstacle avoidance settings. The conditions were set as follows: desired depth = 1·7 m, speed = 0·25 m/sec, k_{az} (gain value of the attractive force) = 0·5, l_z (condition for the switching of attractive function) = 2 m; k_{rh} (gain value of the repulsive force) = 0·8 and h_0 (range of the repulsive field) = 5 m. It was first conducted without obstacle avoidance settings, and the results were as shown in Figure 15. The red line shows that the AUV moved at a fixed depth throughout the course, including when it moved over the obstacle. According to the altitude data, the AUV passed the obstacle at a point only 0·7 m above the obstacle; collision would have occurred had the AUV dived slightly deeper.

https://doi.org/10.1017/S0373463318000589 Published online by Cambridge University Press

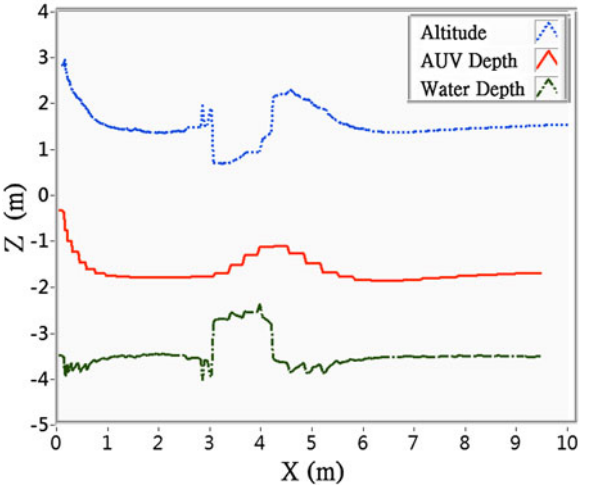

Figure 17. Cruising at 0·3 m/sec at desired altitude of 1·5 m.

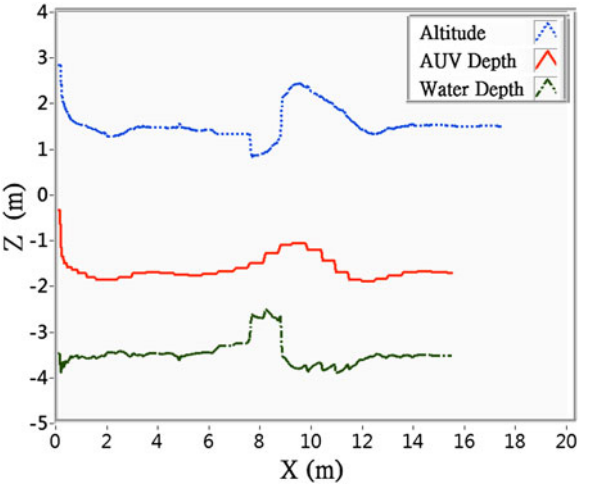

Figure 18. Cruising at 0·4 m/sec at desired altitude of 1·5 m.

The trial was repeated with the same conditions, but with obstacle avoidance settings. The results were as shown in Figure 16, which indicates that in the beginning, the attractive force was greater than the repulsive force, hence the AUV dived down to the desired depth, until it came within range of the obstacle, at which point the decreased altitude and intensified repulsive force changed the direction of the resultant force, altered the depth-control command, and caused the AUV to veer upward to prevent collision with the obstacle, until it successfully passed the obstacle, after which the increased altitude and decreased repulsive force brought the AUV back to the desired depth.

4.4. *Altitude control trial.* The purpose of the altitude control trial was to verify the AUV's bottom-following capability. The trial was conducted with different AUV speeds, and the results are shown in Figures 17 and 18. The maximum operating depth was set to

https://doi.org/10.1017/S0373463318000589 Published online by Cambridge University Press

be 5 m. At the start, the attractive force brought the AUV down to the desired altitude, after which the AUV cruised at the fixed altitude until it came within range of the obstacle; then the increased repulsive force compelled the AUV to ascend to maintain its distance from the obstacle. The results indicate that the AUV passed the altitude control trial because it was capable of following the contours of the terrain at a fixed altitude, and the trajectory of its movement maintained a constant distance from the profile of the bottom.

5. CONCLUSION. This study proposed an APFM-based H∞ control approach for obstacle-avoidance (depth control) and bottom-following (altitude control) algorithms. The obstacle avoidance algorithm sets a desired depth to prevent the AUV from colliding with the seabed or an obstacle. Although it cannot solve the problem of local minima, which can render the AUV unable to reach its destination when the desired depth is too close to the seabed, this limitation promotes safety and ensures that the AUV will not hit the seabed. The altitude control algorithm sets a maximum operating depth to prevent the AUV from diving so far that it exceeds the limit of its structural strength when following the seabed. Simulation and laboratory trial results show that the AUV was able to meet the expected performance requirement by obeying the safety restrictions on the desired depth and altitude for all seabed terrain without any collisions. Moreover, the H∞ controller was capable of precision navigation, thus verifying the feasibility and effectiveness of the proposed combination of H∞ control and the APFM. The follow-up to this study will consider underwater signal interference, and will emphasise how to eliminate sensor noise, enhance measurement accuracy, and prevent misjudgement of signals. The results will be tested in sea trials to verify their feasibility.

REFERENCES

Antonelli, G., Chiaverini, S., Finotello, R., and Schiavon, R. (2001). Real-time path planning and obstacle avoidance for RAIS: an autonomous underwater vehicle. *IEEE Journal of Oceanic Engineering*, **26**(2), 216–227.

Cheng, C.L., Zhu, D.Q., Sun, B., Chu, Z.Z., Nie, J.D. and Zhang, S. (2015). Path planning for autonomous underwater vehicle based on artificial potential field and velocity synthesis. *IEEE 28th Canadian Conference on Electrical and Computer Engineering*, 717–721.

Creuze, V. and Jouvencel, B. (2002). Avoidance of underwater cliffs for autonomous underwater vehicles. *Proceedings of the 2002 IEEE/RSJ International Conference on Intelligent Robots and Systems*, 793–798.

Ding, F.G., Jiao, P., Bian, X.G. and Wang, H.J. (2005). AUV local path planning based on virtual potential field. *Proceedings of the IEEE International Conference on Mechatronics & Automation*, **4**, 1711–1716.

Doyle, J.C., Glover, K., Khargonekar, P.P. and Francis, B.A. (1989). State-space solutions to standard H2 and H∞ control problems. *IEEE Transactions on Automatic Control*, **34**(8), 831–847.

Fang, M.C., Chang, P.E. and Luo, J.H. (2006). Wave effects on ascending and descending motions of the autonomous underwater vehicle. *Ocean Engineering,* **33**, 1972–1999.

Fang, M.C., Hou, C.S. and Luo, J.H. (2007). On the motions of the underwater remotely operated vehicle with the umbilical cable effect. *Ocean Engineering*, **34**, 1275–1289.

Fang, M.C., Wang, S.M., Wu, M.C. and Lin, Y.H. (2015). Applying the self-tuning fuzzy control with the image detection technique on the obstacle-avoidance for autonomous underwater vehicles. *Ocean Engineering*, **93**, 11–24.

Feng, Z. and Allen, R. (2002). H∞ autopilot design for an autonomous underwater vehicle. *Proceedings of the 2002 International Conference on Control Applications*, 350–354.

Gao, J., Xu, D., Zhao, N. and Yan, W. (2008). A potential field method for bottom navigation of autonomous underwater vehicles. *Proceedings of the 7th World Congress on Intelligent Control and Automation*, 7466–7470.

Gao, Y., Wei, Z.Q., Gong, F.X., Yin, B. and Ji, X.P. (2013). Dynamic path planning for underwater vehicles based on modified artificial potential field method. *Fourth International Conference on Digital Manufacturing & Automation*, 518–521.

Ge, S.S. and Cui, Y.J. (2000). New potential functions for mobile robot path planning. *IEEE Transactions on Robotics and Automation*, **16**(5), 615–620.

Ge, S.S., and Cui, Y.J. (2002). Dynamic motion planning for mobile robots using potential field method. *Autonomous Robots*, **13**, 207–222.

Hanumant, S. (1995). Sonar mapping with the Autonomous Benthic Explorer (ABE). *Proceedings of the 9th International Symposium on Unmanned Untethered Submersible Technology*, 367–375.

Hwang, C.N. (1993). Formulation of H2 and H∞ optimal control problems – a variational approach. *Journal of the Chinese Institute of Engineers*, **16**(6), 853–866.

Hwang, C.N. (2002). The integrated design of fuzzy collision-avoidance and H∞-autopilots on ships. *The Journal of Navigation*, **55**, 117–136.

Kaminer, I., Pascoal, A.M. Silvestre, C.J. and Khargonekar, P.P. (1991). Control of an underwater vehicle using H-infinity synthesis. *Proceedings of the 30th IEEE Conference on Decision and Control*, 2350–2355.

Kanakakis, V., Valavanis, K.P. and Tsourveloudis, N.C. (2004). Fuzzy-logic based navigation of underwater vehicles. *Journal of Intelligent and Robotic Systems*, **40**, 45–88.

Khatib, O. (1986). Real-time obstacle avoidance for manipulators and mobile robots. *International Journal of Robotics Research*, **5**(1), 90–98.

Khosla, P. and Volpe, R. (1988). Superquadratic artificial potentials for obstacle avoidance and approach. *Proceedings of the IEEE Conference on Robotics and Automation*, 1778–1784.

Koren, Y. and Borenstein, J. (1991). Potential field methods and their inherent limitations for mobile robot navigation. *IEEE International Conference on Robotics and Automation*, **2**, 1398–1404.

Logan, C.L. (1994). A comparison between H_infinity/Mu_synthesis control and sliding mode control for robust control of a small autonomous underwater vehicle. *Proceedings of the 1994 Symposium on Autonomous Underwater Vehicle Technology*, 399–416.

Moreira, L. and Soares, C.G. (2008). H2 and H∞ Designs for diving and course control of an autonomous underwater vehicle in presence of waves. *IEEE Journal of Oceanic Engineering*, **33**(2), 69–88.

Petrich, J. and Stilwell, D.J. (2011). Robust control for an autonomous underwater vehicle that suppresses pitch and yaw coupling. *Ocean Engineering*, **38**(1), 197–204.

Saravanakumar, S. and Asokan, T. (2013). Multipoint potential field method for path planning of autonomous underwater vehicles in 3D space. *Intelligent Service Robotics*, **6**(4), 211–224.

Rimon, E. and Koditschek, D.E. (1992). Exact robot navigation using artificial potential functions, Robotics and Automation. *IEEE Transactions on Robotics and Automation*, **8**(5), 501–518.

Yin, L. and Yin, Y. (2008). An improved potential field method for mobile robot path planning in dynamic environments. *Proceedings of the 7th World Congress on Intelligent Control and Automation*, 4847–4852.